AE370 Group Project 2

Nikita Kovalov*, Daniel Song†, Oliver Walsh‡, and Brian Wu§
University of Illinois at Urbana-Champaign, Champaign, Illinois, 61820

I. IBVP Introduction

A. Engineering Context and Motivation

Aerospace engineers employ lightweight, flexible lifting surfaces to optimize aerodynamic performance under various loading conditions and system applications. These surfaces undergo substantial bending and vibration during operation, where excessive deflections can prove detrimental to performance and structural stability. This project aims to model flexible wing responses under applied loading conditions to predict wingtip deflections and vibration levels under operational use. The resultant findings of this report are relevant to the design and fabrication of an aerodynamic model, as outlined in I.B. This project specifically employs a one-dimensional Euler-Bernoulli beam to model aircraft wing behavior under transverse vibration conditions inspired by real-world applications. This approach allows for the identification and analysis of resonance and transient responses to loads and control inputs, as described in I.C.

B. Guiding Questions

This project aims to answer the following questions through approximation of the guiding IBVP described in I.C:

1) **What is the scale of wingtip deflections under the applied loading conditions? How do these deflections evolve with time?** The scope of this project includes the simulation of the time-dependent transverse deflections of the idealized beam. The results of this analysis are directly relevant to ensure that maximum tip deflections obey external design constraints, such as clearance considerations and structural rigidity.
2) **How do the structural parameters influence the natural frequencies and vibration characteristics?** The bending stiffness, denoted EI, and length, denoted L, serve as the key design parameters for this project, where the results of this analysis help inform material selection and lifting surface design by engineers. This specific analysis primarily aims to reduce resonant responses to the relevant excitation sources.
3) **How does damping influence vibration decay and the return to trim following disturbances?** The investigation of this question includes identifying the relationship between the damping coefficient, denoted c_d, and rate of oscillatory decay, which is similarly relevant to lifting surface design. The results of this analysis are therefore a further examination of (2).

C. Mathematical Formulation

Introduction and Governing Equation

This project aims to quantify and analyze the state properties of a flexible aircraft wing under loading conditions that are inspired by real-world operational use. The flexible wing under observation is idealized as a slender, one-dimensional Euler-Bernoulli beam for approximate analysis. This idealization enables the use of IBVP solution strategies by design.

The idealized wing is aligned along the spanwise coordinate x with length L. The base of the wing at $x = 0$ is clamped, simulating a static airframe, while the wingtip at $x = L$ is subject to the resultant deflections imposed by the aircraft's operating conditions, such as gusts of wind. The wing's transverse deflection from its undeformed equilibrium position is denoted by $w(x, t)$ for spanwise position $x \in (0, L)$ and $t > 0$. The damped Euler–Bernoulli beam equation governs this analysis and is given below by Equation 1.

$$\rho A w_{tt}(x,t) + c_d w_t(x,t) + EI w_{xxxx}(x,t) = q(x,t) \tag{1}$$

*Undergraduate Student, Department of Aerospace Engineering
†Undergraduate Student, Department of Aerospace Engineering
‡Undergraduate Student, Department of Aerospace Engineering
§Undergraduate Student, Department of Aerospace Engineering

The governing equation is comprised of four terms:

1) $\rho A w_{tt}(x,t)$ serves as the inertial term, where ρA is the mass per unit length of the beam and w_{tt} is the transverse acceleration, $\delta^2 w/\delta t^2$.
2) $c_d w_t(x,t)$ serves as the damping term, where c_d is the damping coefficient per unit length and w_t is the transverse velocity.
3) $EIw_{xxxx}(x,t)$ serves as the elastic term, where EI is the aforementioned bending stiffness. The bending moment of the beam is computed according to $M(x,t) = -EIw_{xx}(x,t)$, where the shear force is given by $V(x,t) = M_x(x,t) = -EIw_{xxx}(x,t)$. The load per unit length is therefore computed as $q_{int}(x,t) = -V_x(x,t) = EIw_{xxxx}(x,t)$, yielding the term employed by the governing equation.
4) $q(x,t)$ serves as the external loading term, which reflects the applied distributed load per unit length.

The physical significance and standard units of these terms and their respective physical parameters are summarized in I.D. This IBVP is therefore represented by a linear relationship with second-order dependence in time and fourth-order dependence in space.

Boundary Conditions

The idealized model employed for this analysis assumes a clamped base root and free tip, as described in the introduction. The mathematical representations of these boundary conditions are therefore described below by Equations 2 and 3, respectively.

$$w(0,t) = 0, \quad w_x(0,t) = 0, \quad t > 0 \tag{2}$$

$$w_{xx}(L,t) = 0, \quad w_{xxx}(L,t) = 0, \quad t > 0 \tag{3}$$

The above boundary conditions specify fixed displacement and slope at the base, enforcing rigid attachment to the airframe, and an unconstrained wingtip experiencing zero applied bending moment or shear force. Although these boundary conditions are idealizations and would not be perfectly accurate in the real-world, they are sufficiently reasonable and maintain the significance of the solution.

Initial Conditions

The idealized model assumes a known initial configuration with prescribed displacement and velocity fields. The wing is initially considered to be at rest with a small prescribed deflection for this analysis. The initial conditions are given below by Equation 4, where $\phi_1(x)$ is a chosen approximation for the first bending mode and α is a small amplitude parameter.

$$w(x,0) = \alpha\phi_1(x), \quad w_t(x,0) = 0, \quad 0 \le x \le L \tag{4}$$

Load Modeling

This project employs two forms of idealized loading, $q(x,t)$, to enable solution of the three questions put forth by I.B. The first case represents uniform step loading along the span, idealizing control inputs, while the second represents wingtip impulsive loading, idealizing localized disturbances such as a gusts of wind.

1) Control inputs are idealized by the relationship $q(x,t) = q_0 H(t)$ for $0 < x < L$, where q_0 is the constant load magnitude and $H(t)$ is the Heaviside step function. This loading would result from a variation in aircraft pitching, for example.
2) Localized disturbances are idealized by the relationship $q(x,t) = q_{imp}(t)\chi_{[x_L, x_L+\Delta x]}(x)$, where $q_{imp}(t)$ is a short duration pulse in time and $\chi_{[x_L, x_L+\Delta x]}(x)$ is an indicator function for the region near the wingtip. $x_L \approx L$ and $\Delta x << L$ for this idealization, where this loading would result from sudden changes in flight conditions, for example.

Mathematical Conclusion

The one-dimensional Euler-Bernoulli beam IBVP employed by this project is dependent on various design parameters, as summarized in I.D. The variation of these parameters enables complex analysis of in-flight wing state properties under the idealized conditions set forth previously. Although this IBVP is intrinsically difficult to solve due to its fourth-order dependence in space, additional assumptions and employment of numerical methods enable the investigation of these properties under varying the various conditions described in I.B.

D. Parameters and Nomenclature

The relevant parameters employed by this project are given below with their respective units and physical significance. The parameters may be further idealized to enable solution of the wingtip behavior, as given by the IBVP.

Symbol	Units	Physical Significance	Employed Value/Range
x	m	Spanwise coordinate	[0m, 1.5m]
t	s	Time	[0s, 10s]
$w(x,t)$	m	Transverse deflection	–
L	m	Beam length	1.5m
ρ	kg/m^3	Density	2700.0kg/m^3
A	m^2	Cross-sectional area	$5{\cdot}10^{-4}$m^2
ρA	kg/m	Mass per unit length	1.35kg/m
E	Pa (N/m^2)	Young's modulus	$70{\cdot}10^9$Pa
I	m^4	Second cross-sectional moment of area	$4.17{\cdot}10^9$m^4
EI	N·m^2	Bending stiffness	$2.92{\cdot}10^2$N·m^2
c_d	N·s/m^2	Damping coefficient per unit	2.0N·s/m^2
$q(x,t)$	N/m	External load per unit length	*Variable*
q_0	N/m	Magnitude of uniform loading	*Variable*
$q_{\text{imp}}(t)$	N/m	Time pulse	133.33N/m
$w_0(x)$	m	Initial deflection	0.005m
$v_0(x)$	m/s	Initial transverse velocity	0m/s
α	m	Initial deflection amplitude	0.005m
$\phi_1(x)$	–	Shape function	–
$H(t)$	–	Heaviside step function	–
$\chi_{[x_L, x_L+\Delta x]}(x)$	–	Wingtip indicator function	–

Table 1 IBVP Parameters

This project employs the subscript notation for partial derivatives as shown in the governing equation and specified conditions, where $w_x = \delta w/\delta x$, for example.

II. Methods

A. Backward Euler Time Integration

Consider the initial value problem

$$\frac{dy}{dt} = f(t,y), \quad y(t_0) = y_0, \tag{5}$$

where $y(t)$ is the unknown solution and f is a given function. The goal of a time-marching method is to approximate $y(t)$ at discrete times $t_n = t_0 + n\Delta t$.

Integrating (5) over a single time step $[t_n, t_{n+1}]$ yields the exact relation

$$y(t_{n+1}) - y(t_n) = \int_{t_n}^{t_{n+1}} f(t, y(t))\, dt. \tag{6}$$

The Backward Euler method is obtained by approximating the integral in (6) using a right-endpoint quadrature rule:

$$\int_{t_n}^{t_{n+1}} f(t, y(t))\, dt \approx \Delta t\, f(t_{n+1}, y(t_{n+1})). \tag{7}$$

Substituting this approximation into (6) and replacing the exact solution with numerical approximations gives

$$y_{n+1} = y_n + \Delta t\, f(t_{n+1}, y_{n+1}), \tag{8}$$

which defines the Backward Euler method.

B. Accuracy, Stability, and Computational Cost Considerations

The Backward Euler method was selected as the time integration scheme for this project based on its accuracy, stability, and computational cost characteristics, particularly in the context of the damped Euler–Bernoulli beam initial boundary value problem.

1. Accuracy

Backward Euler is a first-order accurate method in time, exhibiting a global truncation error of $O(\Delta t)$. While this level of temporal accuracy is lower than that of higher-order methods such as the trapezoidal rule, it is sufficient for capturing the qualitative and quantitative behaviors of interest in this study, including transient vibration response, oscillation decay, and steady-state deflection. Furthermore, the first-order convergence rate is clearly reflected in the temporal convergence studies, which demonstrate error scaling consistent with theoretical expectations. As a result, Backward Euler provides a reliable baseline method against which higher-order schemes can be compared.

2. Stability.

Stability considerations are of primary importance for the Euler–Bernoulli beam equation. The presence of a fourth-order spatial derivative leads to a stiff system after spatial discretization, with high-frequency bending modes introducing large negative eigenvalues into the semi-discrete system. For such stiff systems, explicit time integration methods require prohibitively small time step sizes to maintain stability.

Backward Euler is an implicit, A-stable method, meaning it remains stable for all time step sizes when applied to linear systems with eigenvalues in the left half of the complex plane. This unconditional stability allows the method to robustly damp high-frequency numerical modes without instability, making it well suited for long-time simulations of damped structural dynamics. In the present context, this stability property ensures that the numerical solution remains bounded and physically meaningful even when moderately large time steps are employed.

3. Computational Cost.

The primary computational cost associated with the Backward Euler method arises from its implicit nature, which requires the solution of a linear system at each time step. For the semi-discrete beam system, this results in a linear solve involving a matrix composed of mass, damping, and stiffness contributions. However, this cost is mitigated by the fact that the system matrix remains constant in time for fixed parameters and uniform time stepping, allowing for efficient reuse of matrix factorizations.

Moreover, the unconditional stability of Backward Euler permits the use of larger time steps than would be feasible with explicit methods, thereby reducing the total number of time steps required to reach a given final time. Consequently, the overall computational cost remains reasonable while maintaining numerical robustness.

4. Method Appropriateness.

In summary, the Backward Euler method offers a favorable balance of robustness, simplicity, and computational efficiency for the study of the damped Euler–Bernoulli beam IBVP. Its unconditional stability makes it particularly well suited for stiff structural dynamics problems, while its modest accuracy is sufficient to capture the key physical behaviors of interest. These properties make Backward Euler an appropriate and effective choice for investigating transient response, vibration decay, and steady-state behavior in the present study.

C. Algorithmic Summary for the Backward Euler Method

This section summarizes how the Backward Euler method is applied to compute the numerical solution of the damped Euler–Bernoulli beam initial boundary value problem as a function of space and time.

1. Spatial Discretization

The spatial domain $x \in [0, L]$ is discretized using a uniform grid with m nodes and spacing $\Delta x = L/(m-1)$. The transverse displacement and velocity fields are approximated at these grid points by vectors

$$\mathbf{w}(t) \approx [w(x_1, t), \ldots, w(x_m, t)]^T, \quad \mathbf{v}(t) \approx [v(x_1, t), \ldots, v(x_m, t)]^T. \tag{9}$$

The fourth spatial derivative w_{xxxx} is approximated using a second-order accurate finite-difference operator D_4 constructed from the standard centered stencil

$$w_{xxxx}(x_i) \approx \frac{1}{\Delta x^4} \left[w_{i-2} - 4w_{i-1} + 6w_i - 4w_{i+1} + w_{i+2} \right] + O(\Delta x^2). \tag{10}$$

The clamped boundary conditions at $x = 0$ are enforced by setting $w_1 = 0$ and eliminating w_0 using the condition $w_x(0) = 0$, which gives $w_0 = w_2$ via a centered difference approximation. Similarly, the free boundary conditions at $x = L$ are enforced by eliminating ghost points w_{m+1} and w_{m+2} using the conditions $w_{xx}(L) = 0$ and $w_{xxx}(L) = 0$, which yield

$$w_{m+1} = 2w_m - w_{m-1}, \quad w_{m+2} = 2w_{m+1} - w_m = 3w_m - 2w_{m-1}. \tag{11}$$

These boundary treatments are incorporated directly into the finite-difference stencils near the boundaries, resulting in a modified operator D_4 that acts on the interior and boundary nodes consistently.

2. Semi-Discrete System

Introducing the velocity variable $\mathbf{v} = \mathbf{w}_t$, the governing equation is rewritten as a first-order system in time:

$$\mathbf{w}_t = \mathbf{v}, \tag{12}$$

$$\mathbf{v}_t = \frac{1}{\rho A} \left(\mathbf{q}(t) - c_d \mathbf{v} - EI\, D_4 \mathbf{w} \right), \tag{13}$$

where $\mathbf{q}(t)$ is the discretized external load vector.

3. Time Discretization

Time is discretized into uniform steps of size Δt, with $t_n = n\Delta t$. Given the numerical solution $(\mathbf{w}_n, \mathbf{v}_n)$ at time t_n, the Backward Euler method advances the solution to time t_{n+1} by solving an implicit system.

Applying Backward Euler to equations (9) and (10) yields

$$\mathbf{w}_{n+1} = \mathbf{w}_n + \Delta t\, \mathbf{v}_{n+1}, \tag{14}$$

$$\mathbf{v}_{n+1} = \mathbf{v}_n + \frac{\Delta t}{\rho A} \left(\mathbf{q}_{n+1} - c_d \mathbf{v}_{n+1} - EI\, D_4 \mathbf{w}_{n+1} \right). \tag{15}$$

To eliminate $\mathbf{w}_{n+1}$ from equation (14), we substitute equation (13) into (14):

$$\mathbf{v}_{n+1} = \mathbf{v}_n + \frac{\Delta t}{\rho A} \left(\mathbf{q}_{n+1} - c_d \mathbf{v}_{n+1} - EI\, D_4 (\mathbf{w}_n + \Delta t\, \mathbf{v}_{n+1}) \right). \tag{16}$$

Rearranging and collecting terms in $\mathbf{v}_{n+1}$ gives the linear system

$$\left[I + \frac{\Delta t}{\rho A} c_d I + \frac{\Delta t^2}{\rho A} EI\, D_4 \right] \mathbf{v}_{n+1} = \mathbf{v}_n + \frac{\Delta t}{\rho A} \mathbf{q}_{n+1} - \frac{\Delta t}{\rho A} EI\, D_4 \mathbf{w}_n. \tag{17}$$

Once $\mathbf{v}_{n+1}$ has been computed by solving this system, the displacement field is updated explicitly using equation (13).

4. Linear System Solution

The system matrix in equation (16) is sparse, symmetric, and positive definite due to the positive damping coefficient and the positive-definite nature of the D_4 operator for the given boundary conditions. The matrix is assembled once at the beginning of the simulation and factored using a direct Cholesky or LU decomposition. This factorization is reused at each time step, requiring only forward and backward substitution to solve for $\mathbf{v}_{n+1}$, which significantly reduces computational cost.

5. Time Marching Procedure

Starting from the prescribed initial conditions $\mathbf{w}_0$ and $\mathbf{v}_0$, obtained by evaluating the initial displacement $w(x,0) = \alpha\phi_1(x)$ and velocity $w_t(x,0) = 0$ at the spatial grid points, this process is repeated for each time step until the desired final time is reached. At each step, quantities of interest such as the wingtip deflection $w(L,t_n)$ and spatial displacement profiles $w(x,t_n)$ are recorded for post-processing and analysis.

6. Verification

The implementation of the Backward Euler method will be verified through temporal and spatial convergence studies presented in Section III. These studies will confirm the expected first-order temporal accuracy and second-order spatial accuracy by demonstrating that the numerical error scales as $O(\Delta t)$ and $O(\Delta x^2)$, respectively, under grid refinement.

7. Summary

In summary, the numerical solution procedure consists of discretizing the beam in space using second-order finite differences, reducing the governing PDE to a stiff system of ordinary differential equations, and advancing this system in time using the Backward Euler method. The implicit nature of the method ensures stable time integration of the stiff semi-discrete system, while the resulting linear system at each time step enables efficient and robust computation of the beam's dynamic response through reuse of a single matrix factorization.

III. Method Implementation

To verify the correctness of the numerical implementation, both temporal and spatial convergence studies are performed using the relative discrete L^2 error norm defined in Equation (18). The error is evaluated at a fixed final time T.

For temporal convergence, the spatial grid is held fixed while the time step Δt is refined. A reference solution W_{ref} is computed on the same spatial grid using a time step $\Delta t_{\text{ref}} = \min(\Delta t)/r$, where r is a refinement factor. Figure 1a and Figure 2a shows the relative error as a function of Δt on log–log axes. The observed convergence rate is approximately first order, consistent with the theoretical $O(\Delta t)$ accuracy of the Backward Euler method.

For spatial convergence, the time step is chosen sufficiently small so that temporal error is negligible, and the spatial grid is refined. A reference solution is computed on a fine grid and interpolated onto coarser grids for comparison. Figure 1b and Figure 2b shows that the error decreases at a rate consistent with second-order spatial accuracy, $O(\Delta x^2)$, as expected from the centered finite-difference approximation of the fourth derivative.

A. Error Convergence Plots for Case 1

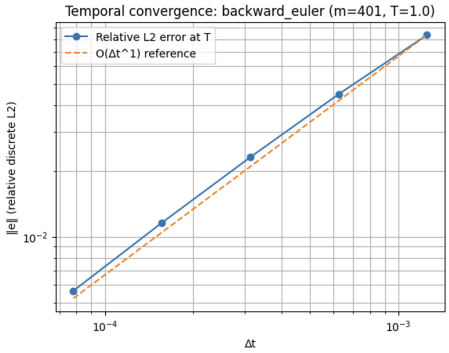

(a) Shown above is the graph of the temporal error convergence of the Euler-Bernoulli beam under loading described in the first case (constant load q_0 over the entire length of the beam).

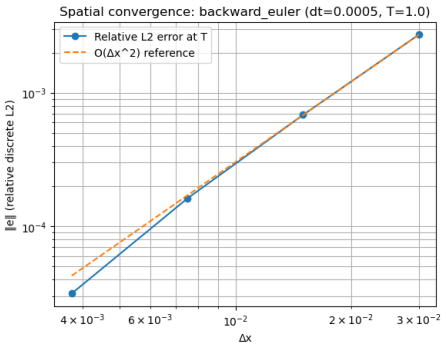

(b) Shown above is the graph of the spatial error convergence of the Euler-Bernoulli beam under loading described in the first case (constant load q_0 over the entire length of the beam).

To accurately study this system, the simulation requires that $\Delta t = 5 \times 10^{-4}$ or less and $\Delta x = 0.00375$ or less.

B. Error Convergence Plots for Case 2

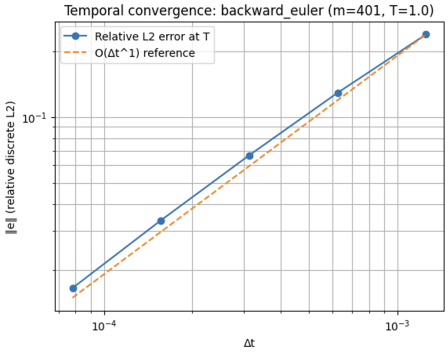

(a) Shown above is the graph of the temporal error convergence of the Euler-Bernoulli beam under loading described in the second case (sudden impulse load $q_{imp}(t)$ at the wingtip).

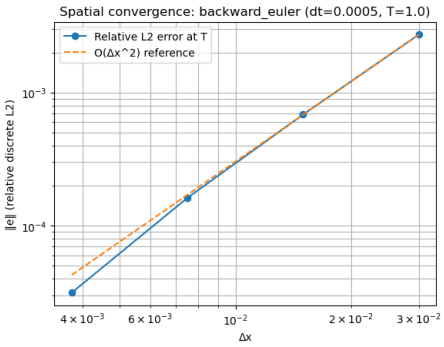

(b) Shown above is the graph of the spatial error convergence of the Euler-Bernoulli beam under loading described in the second case (sudden impulse load $q_{imp}(t)$ at the wingtip).

To accurately study this system, the simulation requires that $\Delta t = 5 \times 10^{-4}$ or less and $\Delta x = 0.00375$ or less.

C. Resolution Requirements

IV. Results

This section presents numerical results that address the guiding questions posed in Section I.B. All results are computed using a fixed time step $\Delta t = 5 \times 10^{-4}$ and a spatial resolution $\Delta x = 0.00375$ to be sufficient for accurate evaluation of the quantities of interest.

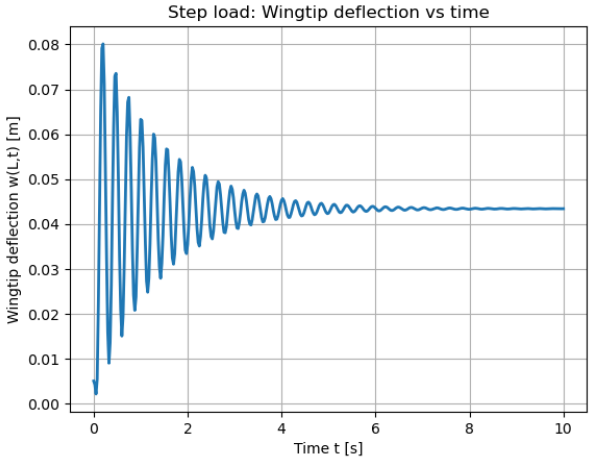

(a) Uniform step loading.

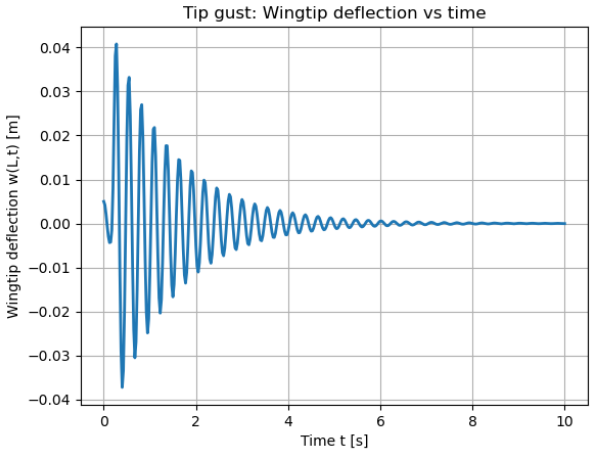

(b) Localized tip-gust loading.

Fig. 3 Wingtip deflection time history $w_{\text{tip}}(t) = w(L,t)$ under (a) uniform step loading and (b) localized gust loading. The step load produces sustained oscillations about a displaced equilibrium position, while the gust produces a purely transient response that decays back toward zero due to damping.

A. Wingtip deflection magnitude and time evolution

The first guiding question asks: *What is the scale of wingtip deflections under the applied loading conditions, and how do these deflections evolve with time?* To address this question, we examine the time history of the wingtip deflection, $w_{\text{tip}}(t) = w(L,t)$, under both uniform step loading and localized gust loading.

Figure 3 shows the wingtip deflection as a function of time for each loading case. Under uniform step loading, the beam exhibits an initial transient followed by sustained oscillations about a displaced equilibrium position, reflecting the static deflection induced by the applied load. In contrast, the localized gust produces a purely transient response that decays back toward zero as damping dissipates energy from the system.

These results demonstrate that different classes of operational loading can lead to fundamentally different wing response behaviors, even when acting on the same structure.

B. Influence of structural stiffness on vibration characteristics

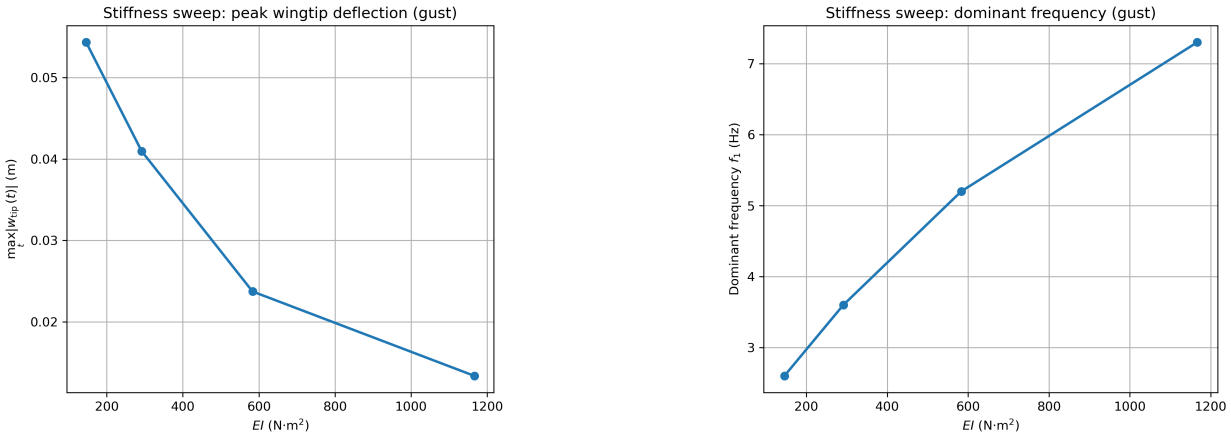

(a) Peak wingtip deflection versus bending stiffness EI.

(b) Dominant vibration frequency versus bending stiffness EI.

Fig. 4 Effect of bending stiffness on the wingtip response under localized gust loading. Increasing stiffness reduces peak deflection while increasing the dominant vibration frequency.

The second guiding question investigates how structural parameters influence vibration behavior, with particular focus on the bending stiffness EI. To quantify this effect, simulations were performed for multiple values of EI while monitoring the wingtip deflection response under localized gust loading.

Figure 4 summarizes the effect of bending stiffness on the dynamic response of the beam. Increasing EI results in a clear reduction in peak wingtip deflection and a corresponding increase in the dominant vibration frequency. This trend is consistent with classical beam theory, in which increased stiffness raises natural frequencies and reduces deformation under applied loads.

The time-domain responses shown in Fig. 6(a) further illustrate this behavior, with increasing stiffness producing smaller-amplitude oscillations and shorter vibration periods following the gust disturbance.

These results highlight the importance of stiffness selection in mitigating resonant responses and limiting excessive deflections in flexible lifting surfaces.

C. Effect of damping on vibration decay and return to trim

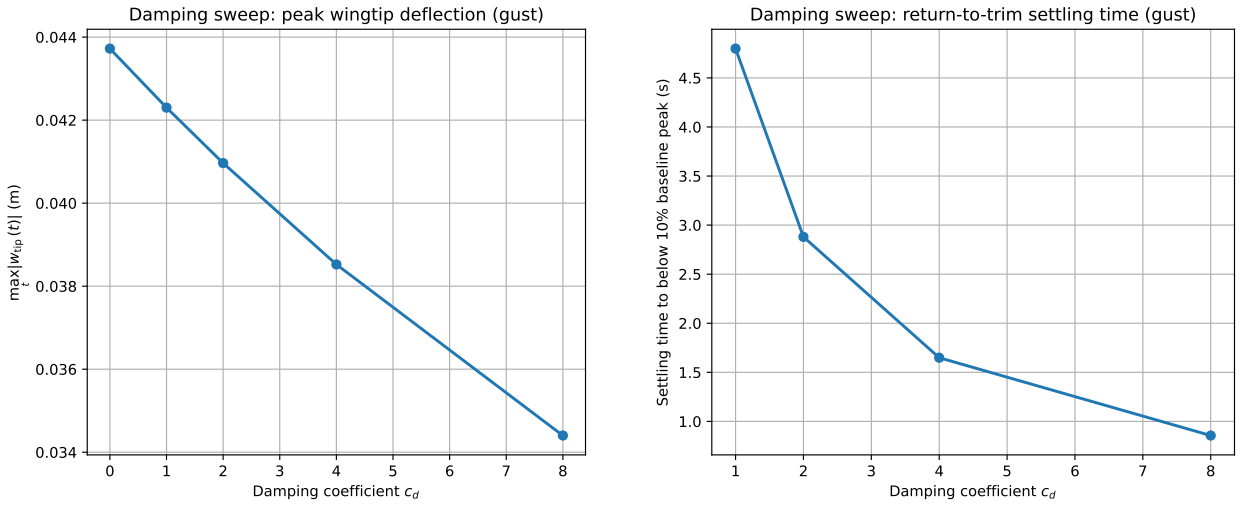

(a) Peak wingtip deflection versus damping coefficient c_d. **(b) Settling time to below 10% of the baseline peak value.**

Fig. 5 Effect of damping on the wingtip response under localized gust loading. Increasing c_d reduces peak deflection and accelerates return to trim.

The third guiding question examines how damping influences vibration decay and the return to trim following transient disturbances. To study this effect, the damping coefficient c_d was varied while monitoring the wingtip response under localized gust loading.

Figure 5 summarizes the effect of damping on the dynamic response. Increasing c_d produces a clear reduction in the peak wingtip deflection (Fig. 5a), indicating that stronger damping suppresses the maximum transient response. In addition, increasing c_d reduces the time required for the response to settle back near equilibrium (Fig. 5b), demonstrating a faster return to trim after the gust disturbance. What's interesting is that the damping coefficient decreases the settling time exponentially, while decreasing peak deflection linearly.

The time-domain responses shown in Fig. 6(b) demonstrate that increasing damping accelerates the decay of oscillations and reduces the time required for the system to return to equilibrium following the gust.

Overall, these results highlight the critical role of damping in limiting transient vibration amplitudes and ensuring rapid recovery from external disturbances in flexible lifting surfaces.

D. Summary of results

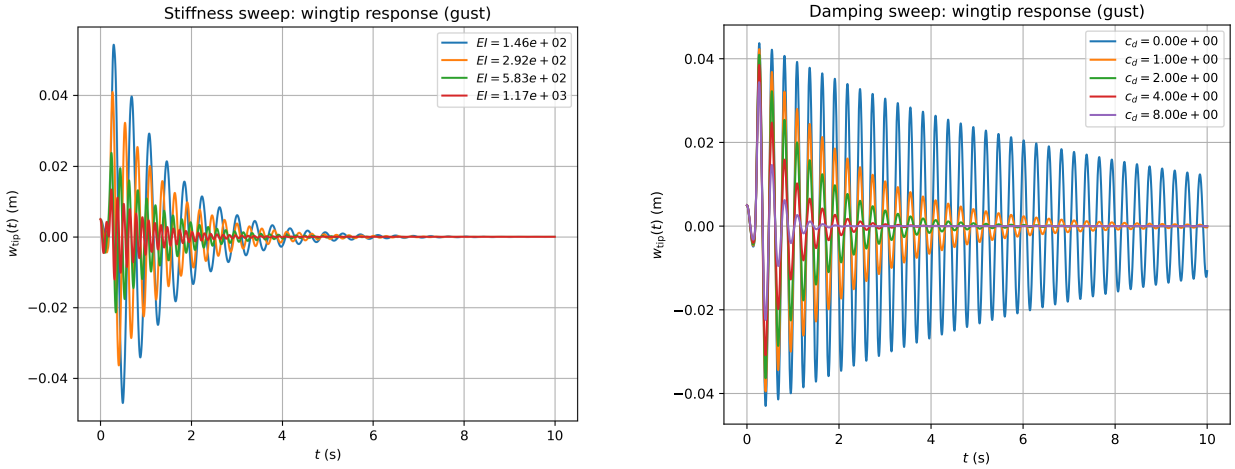

(a) Effect of bending stiffness EI on wingtip response.

(b) Effect of damping coefficient c_d on wingtip response.

Fig. 6 Comparison of wingtip deflection time histories under localized gust loading. Increasing stiffness reduces response amplitude and increases oscillation frequency, while increasing damping accelerates decay of oscillations and return to trim.

Overall, the numerical results demonstrate that the damped Euler–Bernoulli beam model captures key features of flexible wing dynamics under idealized operational loading. Wingtip deflections are strongly dependent on load type, stiffness, and damping, with each parameter playing a distinct role in shaping the transient and steady-state response. These trends provide physically meaningful insight into the design trade-offs involved in flexible lifting surface applications.

Individual Roles and Responsibilities

Nikita Kovalov

Nikita's individual contributions included the results analysis and producing plots to address the vibrational characteristics of the beam posed in the problem statement in Section I. Specifically, Nikita interpreted results of the wingtip deflection over time, the influence of structural stiffness on vibrational characteristics, and the effect of damping on vibration decay and return to trim.

Daniel Song

Daniel's individual responsibilities included the method implementation, producing both the temporal and spatial error convergence plots, and producing the wingtip deflection over time plots. Daniel also set up the GitHub repository to organize the code structure and ensured the report met all requirements through a thorough review.

Oliver Walsh

Oliver's individual responsibilities included the selection of the initial boundary value problem and the definition of the problem statement, more generally the completion of Section I. Additionally, Oliver participated in quality reviews ahead of submissions and verified the computational implementation of the selected method and IBVP.

Brian Wu

Brian's individual responsibilities included the method selection, derivation, and its algorithmic summary to demonstrate how it marches the solution temporally and spatially. Specifically, Brian derived the backward Euler method and justified it's selection through a holistic overview of it's accuracy, stability, and computational cost.

Reproducibility

Link to GitHub to reproduce all results in this report linked here. If the link doesn't work you can try copy and pasting this directly: https://github.com/dssong2/ae370-project2

Acknowledgments

ChatGPT (OpenAI, GPT-5) was used to assist in drafting and refining sections of this report, including improving clarity of explanations, formatting equations in LaTeX, and organizing descriptions of the numerical methods used. It was also used to help structure code documentation and interpret convergence results in a clear and concise manner. All simulations, data analysis, and conclusions were performed and verified independently by the authors.